catalysts

MDPI

Article

NO Reduction Reaction by Kiwi Biochar-Modified MnO_2 Denitrification Catalyst: Redox Cycle and Reaction Process

Hao Fan [1], Zhenxing Shen [1,*], Xiuru Wang [1], Jie Fan [1], Jian Sun [1] and Jiaxiang Sun [2]

[1] Xi'an Key Laboratory of Solid Waste Recycling and Resource Recovery, Department of Environmental Sciences and Engineering, Xi'an Jiaotong University, Xi'an 710049, China
[2] Instrumental Analysis Center of Xi'an Jiaotong University, Xi'an Jiaotong University, Xi'an 710049, China
* Correspondence: zxshen@mail.xjtu.edu.cn

Abstract: NO is a major environmental pollutant. MnO_2 is often used as a denitrification catalyst with poor N_2 selectivity and weak SO_2 resistance. Kiwi twig biochar was chosen to modify MnO_2 samples by using the hydrothermal method. The NO conversion rates of the biochar-modified samples were >90% at 125–225 °C. Kiwi twig biochar made the C2MnO_2 sample with a larger specific surface area, a higher number of acidic sites and O_β/O_α molar ratio, leading to more favorable activity at high temperatures and better SO_2 resistance. Moreover, the inhibition of the NH_3 oxidation reaction and the $Mn^{3+} \rightarrow Mn^{4+}$ process played a crucial role in the redox cycle. What was more, Brønsted acidic sites present on the C1MnO_2 sample participate in the reaction more rapidly. This study identified the role of biochar in the reaction process and provides a reference for the wide application of biochar.

Keywords: kiwi twigs; oxygen vacancy; selective catalytic reaction; reaction process; high-value utilization

check for updates

Citation: Fan, H.; Shen, Z.; Wang, X.; Fan, J.; Sun, J.; Sun, J. NO Reduction Reaction by Kiwi Biochar-Modified MnO_2 Denitrification Catalyst: Redox Cycle and Reaction Process. *Catalysts* **2022**, *12*, 870. https://doi.org/10.3390/catal12080870

Academic Editor: Carlo Santoro

Received: 30 June 2022
Accepted: 29 July 2022
Published: 7 August 2022

1. Introduction

The implementation of the ultralow emission policy for power plants in China has achieved initial success, and the pollution emission standards of other NO sources have been lowered as well [1,2]. In the Emission Standard of Air Pollutants for Iron Smelt Industry released in 2012, the NO emission limit of the iron-making industry was set at 300 mg·m^{-3}. In 2021, the NO emission limits of the sintering process and hot blast furnace were set at 50 and 150 mg·m^{-3}, respectively, in the consultation draft of the Emission Standard of Air Pollutants for Iron and Steel Industry released by Jiangsu Province. NO not only adversely affects cell division and genetic information, but also causes lung and bronchial diseases [3]. Moreover, NO is a precursor of nitric and nitrous acid in acid rain and participates in the formation of particulate matter [4,5]. Under ultraviolet light, NO interacts with carbon and oxygen compounds in the atmosphere to generate photochemical smog and ozone [6].

In the last decades, selective catalytic reduction (SCR) with NH_3 (NH_3-SCR) for NO conversion has been regarded as a promising technology to remove NO [7–9]. V_2O_5–WO_3/TiO_2 is the most widely investigated commercial denitration (deNO) catalyst within the temperature range of 300–400 °C, but the use of V_2O_5–WO_3/TiO_2 is limited by its thermal deactivation and vanadium species volatilization at high temperatures [10]. In addition, the practical application of NH_3-SCR technology is limited due to the lower temperature of flue gas released from the steel industry than that released from coal-fired power plants [11]. Therefore, a new denitrification catalyst that exhibits satisfactory activity at low temperatures and has a wide temperature window is required.

Transition metals are widely used in various catalytic reactions because of their satisfactory electron transport properties and availability [12–14]. Among them, the Mn series of denitration catalysts have attracted increasing research attention because of their satisfactory activity at low temperatures [15–18]. Zhang et al. synthesized MnO_2 with an

interlayer Ce^{3+} cation with favorable NH_3-SCR catalytic activity (over 90%) at 80–200 °C because of the easy supply of labile oxygen species [19]. However, with an increase in temperature, bridged oxygen captures more H atoms on NH_3, generates N atoms, and then reacts with NO to generate N_2O, resulting in the side reaction of NH_3 oxidation [20–22]. To improve the N_2 selectivity, in our previous work, a $FeMnO_2$ catalyst was obtained with good NH_3-SCR activity (over 90% at 125–225 °C), indicating that the surface properties of MnO_2 can be modified by adding other substances [23]. Meanwhile, many studies have proved that biochar, a carbon-rich material, can improve catalytic activity [24,25]. Biochar materials not only possess a large specific surface area [26], which can improve the distribution of active sites and adsorb more reactants [27]. Chen et al. reported a MnO_2 composite modified with samarium and biochar that exhibited a NO conversion of 85% at 200 °C [28]. Furthermore, Yang et al. indicated that a certain surface area and a smaller pore size of biochar played a significant role in the denitration process [29]. In addition, kiwi twigs can increase the specific area of the biochar-modified catalyst and enhance catalyst activity, because they possess abundant water transport channels and pores [30]. Therefore, it is expected that biochar can change the surface properties of a MnO_2 catalyst and increase the specific surface area of the catalyst.

In this paper, we synthesized a kiwi twig biochar-modified MnO_2 catalyst by using a one-step hydrothermal reaction. In this study, we investigated the effect of biochar on the MnO_2 denitrification catalyst by examining the catalyst morphology, element valence state, acid position, and reaction process. The results of this study can provide new insights into employing biochar as a catalyst modifier in chemical reactions.

2. Results and Discussion

2.1. Crystal Morphology and Structure

The crystal structure of the as-prepared samples was investigated through PXRD (Figure 1a). A peak around 20° to 30° was related to amorphous carbon [31]. This finding indicated that the kiwi twig biochar had amorphous carbon and was partially graphitized. This result was further validated through Raman spectroscopy. Peaks at 1346–1350 cm^{-1} and 1598–1604 cm^{-1} were assigned to D and G peaks [32,33], as presented in Figure 1c. The D and G peaks were associated with edge defects and highly ordered graphite, respectively. The Raman I_D/I_G ratios of intensity were calculated to determine the degree of disorder of samples [34]. The I_D/I_G ratios for the $C1MnO_2$ and $C2MnO_2$ samples were 1.0 and 0.97, respectively, indicating that the two samples had similar degrees of disorder and lattice defects.

Similar diffraction peaks appearing at 37.1°, 42.4°, 42.5°, and 56.1° (Figure 1a) were assigned to the (100), (101), and (102) crystal planes of ε-MnO_2 (PDF#30-0820) [35], respectively, indicating that these two samples possessed the same ε-MnO_2 crystal phase. Moreover, the peak of the $C2MnO_2$ sample at 42.5° increased by 0.1°, demonstrating that the (102) crystal plane of the $C2MnO_2$ sample was affected by macroscopic residual stress. The morphology of the samples was obtained through FE-SEM (Figure 2). The two samples exhibited similar morphology; both MnO_2 nanorods and carbon materials were observed. In addition, thermogravimetric analysis was performed to evaluate the thermal stability of the catalysts. The weight loss of the samples was approximately 0.7% at a temperature of <180 °C because of water desorption [36] and approximately 0.8% between 180 and 350 °C, indicating that the sample was stable in the NH_3-SCR reaction temperature range.

The specific surface area and pore size distribution of the catalysts were measured through N_2 adsorption and desorption isotherms (Figure 1b and Figure S1 and Table 1). All the samples were determined to be type IV(a) according to the IUPAC classification denitration, indicating that the products had a mesopores structure [37]. Concurrently, the pore size distribution was mainly concentrated between 30 and 80 nm. The specific surface areas of the $C1MnO_2$ and $C2MnO_2$ samples were 36.48 and 119.74 $m^2 \cdot g^{-1}$, and their pore volumes were 0.18 and 0.17 $cm^3 \cdot g^{-1}$, respectively.

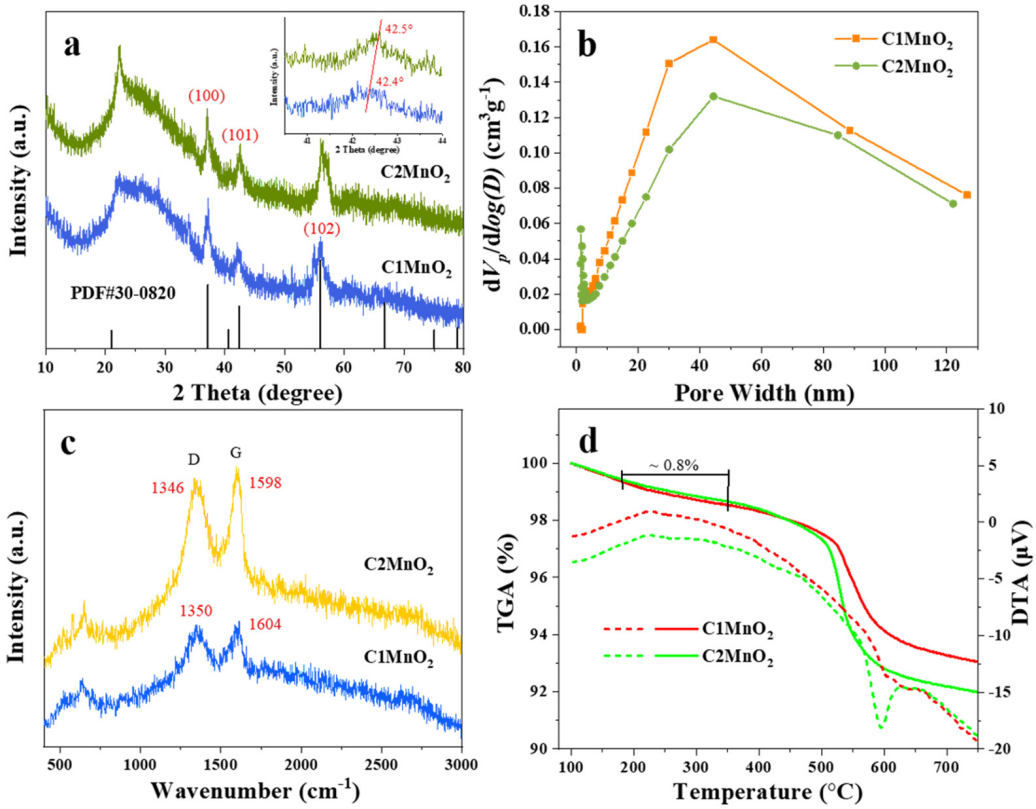

Figure 1. (**a**) XRD patterns, (**b**) pore size distribution from BJH algorithm, (**c**) Raman spectra, (**d**) TGA (Solid lines) and DTA (dotted lines) curves of $C1MnO_2$ and $C2MnO_2$ composite catalysts.

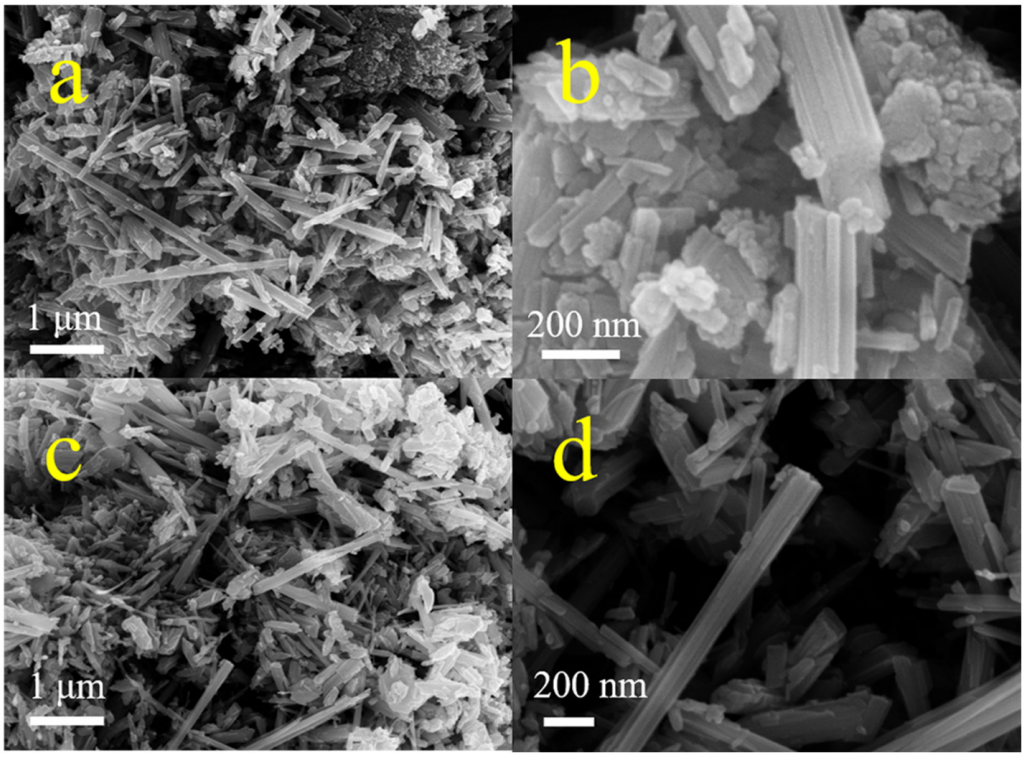

Figure 2. FESEM images of $C1MnO_2$ (**a**,**b**) and $C2MnO_2$ (**c**,**d**) catalysts.

Table 1. Specific surface area, total pore volume, pore size (BJH), Raman data and different atomic percentage ratios of samples.

Samples	S_{BET} ($m^2 \cdot g^{-1}$)	V_{total} ($cm^3 \cdot g^{-1}$)	Pore Size (nm)	I_D/I_G	Mn^{4+}/Mn^{3+}	$O_\alpha/(O_\alpha + O_\beta)$
$C1MnO_2$	36.48	0.17	185.47	1.01	1.77	0.43
$C2MnO_2$	119.74	0.18	59.93	0.97	1.72	0.46

2.2. NH_3-SCR Activity

NH_3-SCR experiments were performed to evaluate the catalytic activity of the samples (Figure 3). Overall, the $C1MnO_2$ and $C2MnO_2$ samples demonstrated similar activity at low temperatures; their NO conversion rates were >90% at 125–225 °C (Figure 3a). The denitrification activity of pure MnO_2 was higher than 90% at 150–175 °C. When the temperature reached 175 °C, the N_2 selectivity of the MnO_2 sample decreased sharply [23]. Therefore, biochar broadened the temperature window of the catalyst. The specific reaction rate of $C1MnO_2$ and $C2MnO_2$ samples at 125 °C were 1.65×10^{-7} and 1.70×10^{-7} $mol \cdot s^{-1} \cdot g^{-1}$, respectively. Furthermore, the de-NO activity of the $C2MnO_2$ sample at >250 °C was higher than that of the $C1MnO_2$ sample. The N_2 selectivity exhibited the same trend. Therefore, the inhibition of the NH_3 oxidation reaction at high temperatures might have led to the higher deNO activity of the $C2MnO_2$ sample. Moreover, after the introduction of SO_2 (Figure 3b), the denitrification activity of the $C2MnO_2$ sample decreased at a lower rate than that of the $C1MnO_2$ sample. After approximately 300 min, the denitrification efficiency of both samples was approximately 70%. When SO_2 was stopped, the denitrification activity of the $C2MnO_2$ sample recovered to approximately 77%, whereas that of the C1 sample rapidly decreased to approximately 57% after brief recovery. Therefore, the $C2MnO_2$ sample had a higher SO_2 resistance than the C1 catalyst, which facilitated the practical application of the catalyst in industry.

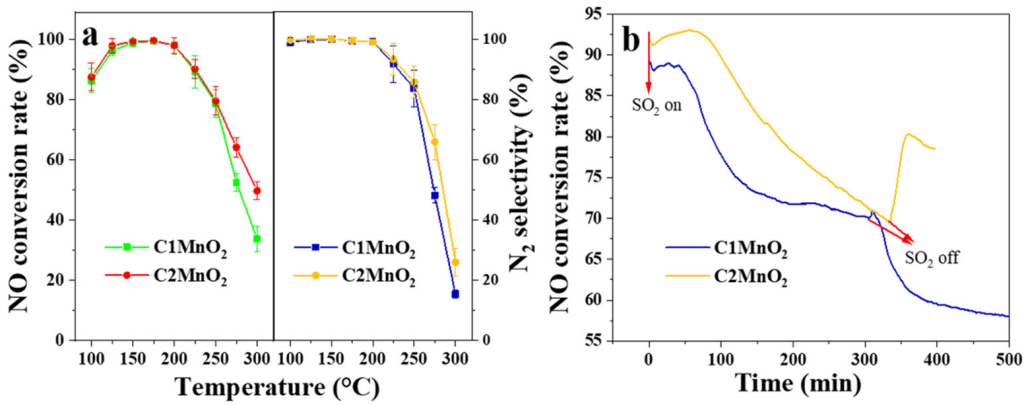

Figure 3. (**a**) NO conversion rate and N_2 selectivity and (**b**) SO_2 resistance under 250 ppmv SO_2 at 175 °C of $C1MnO_2$ and $C2MnO_2$ samples.

The NO conversion rate of the $C2MnO_2$ sample was higher than that of the $C1MnO_2$ sample, especially SO_2 resistance. The surface acidity and redox property of the catalysts were determined to understand the difference in activity.

2.3. Surface Acidity

The adsorption of NH_3 on acid sites is a prerequisite for the occurrence of the NH_3-SCR reaction. Therefore, the acid content and acidity of the catalyst are crucial. In this study, we used NH_3-TPD to characterize the acid content and acid strength and employed in situ DRIFTS to characterize the type of acid sites in the samples. As depicted in Figure 4a, the acid strength of the $C2MnO_2$ sample was weaker than that of the $C1MnO_2$ sample. The desorption peaks of the samples at 194 and 204 °C were assigned to weak acid sites,

and those at 261 and 282 °C were attributed to medium–strong acid sites [38]. The total acid content of the $C2MnO_2$ sample was 1.39 times higher than that of the $C1MnO_2$ sample. In addition, the weak and medium–strong acid contents of the $C2MnO_2$ sample were 1.35 times and 1.58 times higher than those of the $C1MnO_2$ sample, respectively (Table 2). With an increase in temperature, the NH_3 adsorbed on the catalyst was oxidized to NO at 285 and 290 °C (Figure 4a). The $C1MnO_2$ sample promoted the NH_3 oxidation reaction, which might be a reason for its weaker activity at high temperatures; this finding is consistent with our previous conjecture. Furthermore, as presented in the results of in situ DRIFTS (Figure 4b), the peak at 1103 cm^{-1} was assigned to NH_3 adsorbed on Lewis sites [28], and peaks at 1034 and 1066 cm^{-1} were ascribed to the deformation mode of coordinated ammonia at Lewis acidic sites [39]. In addition, peaks at 1354 and 1359 cm^{-1} belonged to the oxidation/deformation species of adsorbed ammonia species [40]. Peaks at 1541 and 1559 cm^{-1} belonged to the asymmetric bending vibration of the N–H bond in the -NH_3 group, which is formed by the decomposition of NH_4^+ chemisorbed on Brønsted acidic sites [41].

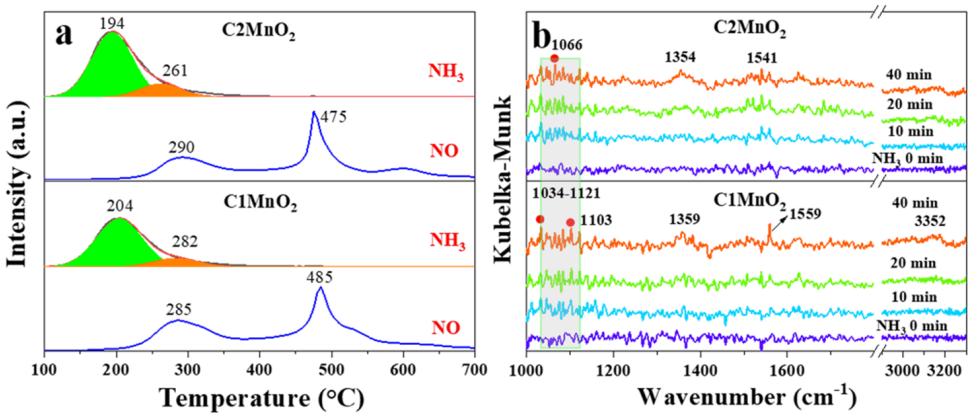

Figure 4. NH_3-TPD and NH_3 oxidization curves (**a**), in situ DRIFTS spectra of NH_3 adsorption (**b**) on $C1MnO_2$ and $C2MnO_2$ samples.

Table 2. Peak area of NH_3-TPD profiles.

$C1MnO_2$			$C2MnO_2$		
Position (°C)	**Area**	**Sum**	**Position (°C)**	**Area**	**Sum**
204	39.3	46.2	194	53.3	64.2
282	6.9		261	10.9	

Sum was the total amount of the weak acid sites and the medium–strong acid sites.

Overall, the two samples possessed both Brønsted and Lewis acidic sites, and the $C2MnO_2$ sample contained more acid sites. However, the intensity of the acidic sites in the $C2MnO_2$ sample was weaker than that in the $C1MnO_2$ sample, indicating that the number of acidic sites plays a crucial role in the NH_3-SCR process.

2.4. Active Sites

The chemical composition and elemental state of the fabricated samples were determined through XPS (Figure 5). Two inconspicuous high-resolution peaks were noted in the C 1s XPS (Figure 5a), indicating that the C element on the surface of catalysts mainly existed as the C–C bond. The XPS of Mn species (Figure 5b) was composed of Mn 2p 3/2 (642.1, 643.4, and 643.5 eV) and Mn 2p 1/2 (653.9 eV) [42]. Among them, the peak at 642.1 eV was ascribed to Mn^{3+} [43], and other peaks were attributed to Mn^{4+} [44]. Furthermore, the ratio of Mn^{4+} to Mn^{3+} in the $C1MnO_2$ sample was 1.77, which was slightly higher than that of the $C2MnO_2$ sample (1.72). By contrast, peaks in the O 1s spectra (Figure 5c) of the as-prepared catalysts suggested the presence of two oxygen species;

the binding energy at 529.7 eV was assigned to lattice oxygen (denoted as O_α) [45], and the binding energy at 531.1 eV was attributed to defect oxide or a low-coordination surface oxygen ion (denoted as O_β) [46]. Subsequently, the O_β/O_α molar ratio of the biochar-modified MnO_2 catalyst was in the order of $C2MnO_2$ (0.84) > $C1MnO_2$ (0.77). O_β was beneficial for promoting the conversion of NO to NO_2 and the release of the H atom from NH_3. Therefore, the higher O_β/O_α ratio of the $C2MnO_2$ sample was responsible for its excellent denitrification performance.

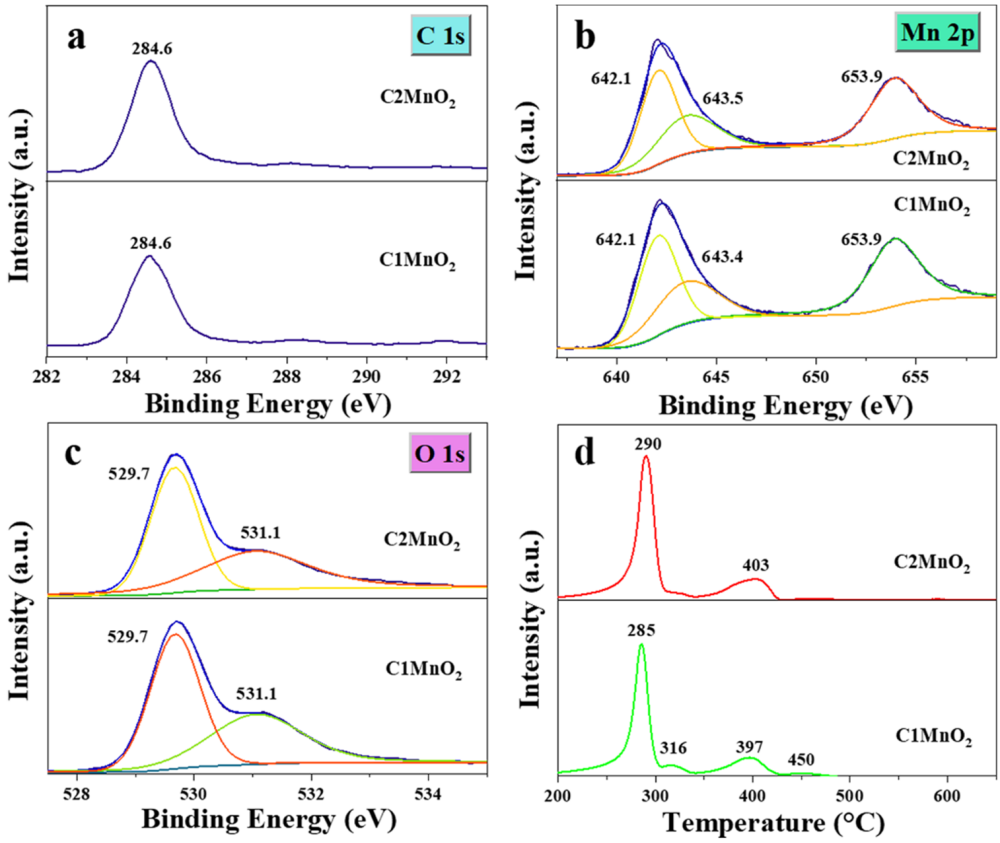

Figure 5. (**a**) C 1s, (**b**) Mn 2p, (**c**) O 1s high-resolution XPS spectra and (**d**) H_2-TPR profiles of $C1MnO_2$ and $C2MnO_2$ samples.

The redox capacity of the catalysts was analyzed through H_2-TPR (Figure 5d). Peaks below 337 °C might be attributable to the reduction of Mn^{4+} to Mn^{3+} [47], and peaks above 365 °C were assigned to the transition from Mn^{3+} to Mn^{2+} [48]. Overall, Mn^{4+} in the $C1MnO_2$ sample was more easily reduced to Mn^{3+}, indicating that Mn^{4+} in the $C1MnO_2$ sample was more likely to participate in the NH_3-SCR reaction corresponding to worse N_2 selectivity. At the same time, Mn^{3+} in the $C2MnO_2$ sample experienced more difficulty reducing to Mn^{2+}, indicating that the Mn^{3+} of the $C2MnO_2$ sample was more easily oxidized to Mn^{4+} compared with that of the $C1MnO_2$ sample to complete the redox cycle in the NH_3-SCR reaction. In addition, the NO conversion rate of the $C2MnO_2$ sample at >250 °C was higher than that of the C1 sample. Therefore, the process $Mn^{3+} \rightarrow Mn^{4+}$ was more crucial than $Mn^{4+} \rightarrow Mn^{3+}$ in the NH_3-SCR reaction.

2.5. Reaction Process

In situ DRIFTS was employed to examine the reaction process of modified samples. As presented in Figure 6a, after the introduction of NO into the reaction system for 25 min, a band peak appeared at approximately 1313 and 1329 cm^{-1}, and sharp peaks appeared at 1596, 1598, 1629 and 1857 cm^{-1}. Peaks at 1596 and 1598 cm^{-1} were associated with bidentate nitrate, and the peak at 1629 cm^{-1} was attributed to bridging bidentate nitrates [49].

Therefore, as shown in Figure 7, NO was adsorbed to the catalyst surface to form a variety of nitrates. In addition, the peak at 1857 cm^{-1} was deemed gaseous or weakly adsorbed NO [50]. However, the band at 1313–1329 cm^{-1} could not be assigned to either catalyst due to a lack of studies.

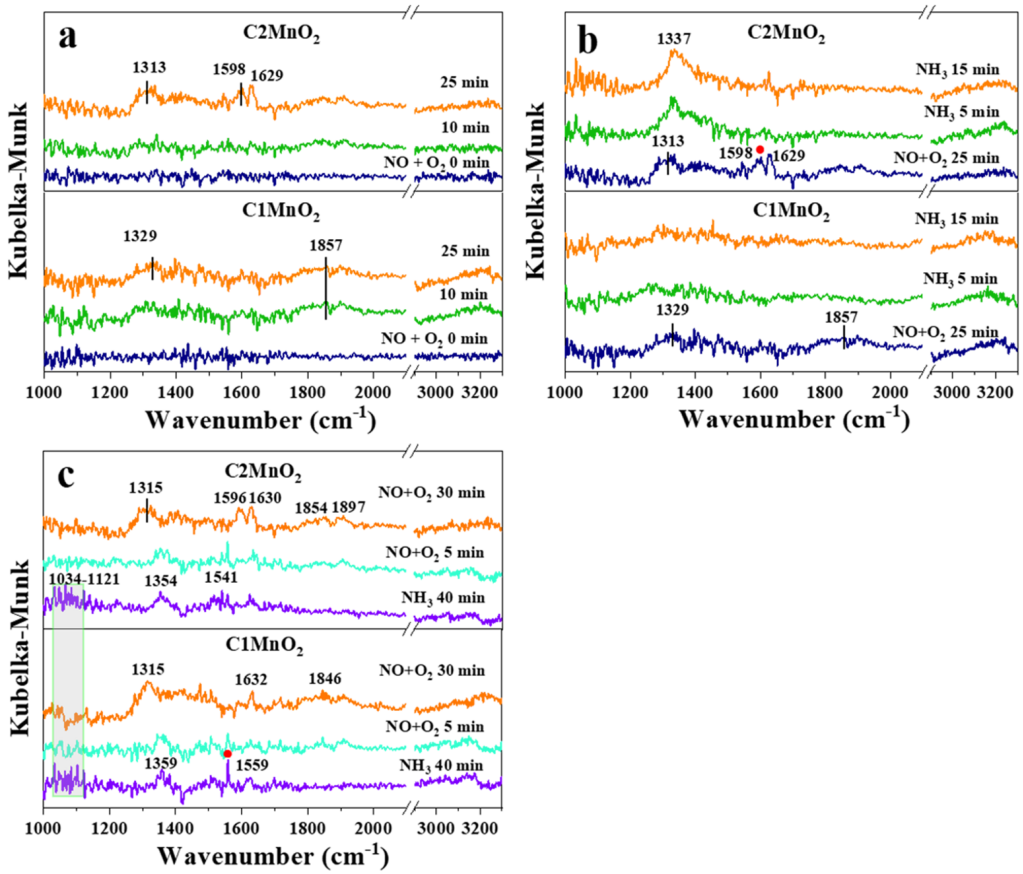

Figure 6. In situ DRIFTS spectra of $C1MnO_2$ and $C2MnO_2$ samples at 150 °C. (**a**) 500 ppmv NO + 5% O_2 were introduced for 25 min, (**b**) 500 ppmv NO + 5% O_2 were absorbed for 25 min and then changed the gas into 500 ppmv NH_3, (**c**) 500 ppmv NH_3 was absorbed for 40 min and then changed the gas into 500 ppmv NO + 5% O_2.

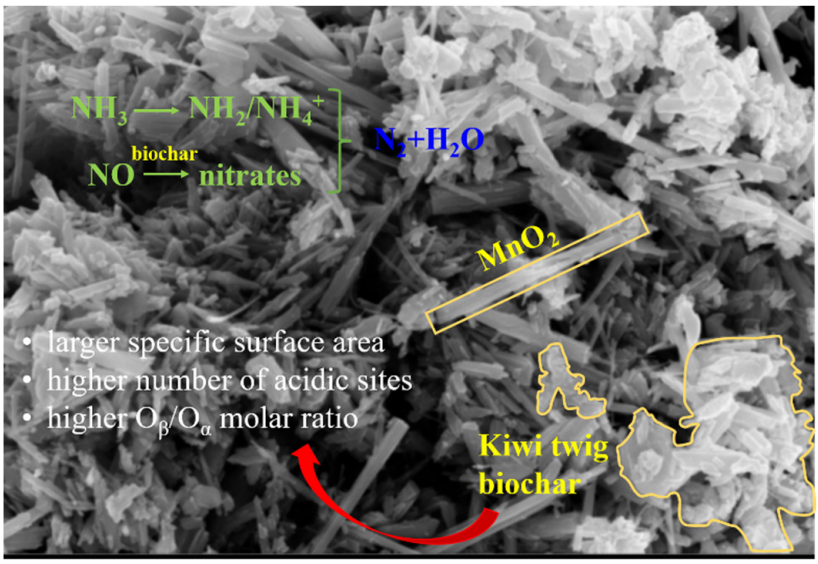

Figure 7. Schematic diagram of the NH_3-SCR process over $C2MnO_2$ sample.

The introduced gas was changed to NH_3 (Figure 6b). In the $C2MnO_2$ sample, NO adsorption peaks at 1598 and 1629 cm^{-1} disappeared after 15 min, indicating that bidentate nitrate and bridging bidentate nitrates were both involved in the NH_3-SCR reaction of the $C2MnO_2$ sample. Moreover, gaseous or weakly adsorbed NO at 1857 cm^{-1} was involved in the reaction. After the saturation of NH_3 (Figure 6c), the introduced gas was changed to NO + O_2; both Brønsted and Lewis acidic sites (NH_4^+ or NH_2) on the samples were involved in the reaction at the same time. As shown in Figure 7, both adsorbed NH_3 and adsorbed NO were reactive species to obtain N_2 and H_2O. Moreover, Lewis acidic sites located on both the samples rapidly participated in the reaction, and Brønsted acidic sites on the $C1MnO_2$ sample were involved in the reaction more easily than those on the $C2MnO_2$ sample.

In summary, adsorbed NH_3 could react with gaseous NO and adsorbed NO in the NH_3-SCR reaction of the $C1MnO_2$ and $C2MnO_2$ samples, with the difference that the Brønsted acidic sites on the $C1MnO_2$ sample could participate in the NH_3-SCR reaction more rapidly.

3. Materials and Methods

3.1. Synthesis of the Catalyst

All reagents used in this study were of analytical grade and purchased from the Sinopharm Chemical Reagent Company (Shanghai, China). Kiwi twig biochar was prepared using two procedures, which were denoted as C1 and C2, respectively. For C1, twigs were treated with KOH (m_{twings}:m_{KOH} = 1:1, m stood for mass) by using the impregnation method. The mixture was then calcinated at 500 °C for 2 h and at 900 °C for 2 h under N_2 atmosphere (heating rate was 5 °C·min^{-1}) with a tubular reactor. After flushing with diluted HCl and deionized water several times, we obtained the final C1 product by drying at 80 °C for 12 h. For C2, twigs were calcined at 500 °C for 2 h and 900 °C for 2 h under N_2 atmosphere. The calcined product was then treated with KOH and calcined again under the aforementioned conditions. After washing and drying, we obtained the final C2 biochar.

The kiwi twig biochar-modified MnO_2 sample was synthesized as follows: 0.316 g of $KMnO_4$ was dissolved in 45 mL of deionized water and stirred for 2 min. Subsequently, 0.05 g of C1 or C2 and 0.25 mL of 37.5% HCl were added into the solution. The solution mixture was transferred into a 100 mL polytetrafluoroethylene autoclave after being stirred for 10 min and was then heated at 140 °C for 12 h. The obtained product was washed several times with deionized water and dried at 80 °C for 12 h. The sample was named $C1MnO_2$ or $C2MnO_2$. The experiment is less dangerous, easy to perform and highly reproducible.

3.2. Catalyst Characterization

The crystal structure of the catalysts was analyzed through powder X-ray diffraction (PXRD, Shimadzu PXRD-6100 (Shimadzu Corporate Management (China) Co., Ltd., Shanghai, China) from 8° to 80° of 2θ at a scanning rate of 2° per minute. The pore size and distribution were measured through N_2 adsorption–desorption by using ASAP 2020 Plus HD88 (Micromeritics (shanghai) instruments Co., Ltd., Shanghai, China), and the samples were pretreated at 250 °C. The morphology of the as-prepared products was observed through field-emission scanning electron microscopy (FE-SEM, ZEISS GeminiSEM 500, Zeiss Optical Instruments (Shanghai) International Trading Co., Ltd., Shanghai, China). The Raman spectra were obtained using inViaQontor (Renishaw Co., Ltd., Gloucestershire, UK). The chemical composition and elemental valence state of different catalysts were determined through X-ray photoelectron spectroscopy (XPS, Thermo Fisher ESCALAB Xi^+ spectrograph, Thermo Fisher Scientific Co., Waltham, MA, USA), which was corrected by C 1s (284.6 eV), and XPS Peak 41 software was used to process the data. Moreover, the acid sites and oxidative reducibility of the catalysts were examined through ammonia temperature-programmed desorption (NH_3-TPD, Thermo 17i NH_3 analyzer, Thermo Fisher Scientific Co., Waltham, MA, USA) and hydrogen temperature-programmed reduction (H_2-TPR, Auto ChemTM II 2920, Micromeritics (shanghai) instruments Co., Ltd., Shanghai, China)

with a heating rate of 10 °C·min^{-1}, and the total carrier gas flow was 50 mL·min^{-1}. In situ diffuse reflectance Fourier transform infrared spectroscopy (in situ DRIFTS) was conducted using the Nicolet iS 50 system (Thermo Fisher Scientific Co., Waltham, MA, USA) by accumulating four scans at 150 °C with a resolution of 4 cm^{-1}; the diameter of the crucible was 5 mm.

3.3. NH_3-SCR Activity

The NO removal efficiency of the C1MnO_2 or C2MnO_2 catalyst was investigated using a NH_3-SCR activity evaluation system equipped with the Thermo Fisher 17i NH_3 detector (Thermo Fisher Scientific Co., Waltham, MA, USA). We used 0.09 g of the composite catalyst in the sampling stage. The original gas contained 500 parts per million by volume (ppmv) NO, 500 ppmv NH_3, and 5% O_2 (N_2 as the equilibrium gas), and 200 ppmv SO_2 was introduced in Poisson experiment at 175 °C. The flow rate was 60 mL·min^{-1}, and space velocity was 15,000 h^{-1}. The NO conversion rate and N_2 selectivity were calculated using the following Equations (1) and (2).

$$X_{NO} = ([NO]_{in} - [NO]_{out})/[NO]_{in} \times 100\% \quad (1)$$

$$S_{N2} = ([NO]_{in} + [NH_3]_{in} - [NO]_{out} - [NO_2]_{out} - [NH_3]_{out} - 2[N_2O])/([NO]_{in} + [NH_3]_{in} - [NO]_{out} - [NO_2]_{out} - [NH_3]_{out}) \times 100\%. \quad (2)$$

4. Conclusions

The kiwi twig biochar-modified MnO_2 samples were successfully synthesized using the hydrothermal method, and the NO conversion rates of the two samples were >90% at 125–225 °C. A larger specific surface area, a higher number of acidic sites, and higher O_β/O_α molar ratio were responsible for more favorable activity at high temperatures and SO_2 resistance in the C2MnO_2 sample. Furthermore, the C2MnO_2 sample inhibited the NH_3 oxidation reaction and promoted the $Mn^{3+} \rightarrow Mn^{4+}$ process, which were crucial for better deNO activity. Moreover, the Brønsted acidic sites on the C1MnO_2 sample could participate in the NH_3-SCR reaction more rapidly. Overall, this study provides new insights into the application of biochar in the catalytic field and the basis for catalyst design by examining the reaction process.

Supplementary Materials: The following supporting information can be downloaded at: https://www.mdpi.com/article/10.3390/catal12080870/s1, Figure S1: N_2 absorption and desorption curves of C1MnO_2 and C2MnO_2 composite catalysts. Figure S2: The complete scan XPS spectra of C1MnO_2 and C2MnO_2 samples.

Author Contributions: Conceptualization, H.F. and Z.S.; methodology, H.F., Z.S. and J.S. (Jiaxiang Sun); investigation, H.F., X.W., J.F., J.S. (Jian Sun) and J.S. (Jiaxiang Sun); data curation, H.F.; writing—original draft, H.F.; funding acquisition, Z.S.; writing—review and editing, Z.S. and J.S. (Jian Sun). All authors have read and agreed to the published version of the manuscript.

Funding: This research was funded by the Science and Technology plan project of Xi'an city, grant number 21NYYF0041, and a grant from State Key Laboratory of Loess and Quaternary Geology, the Chinese Academy of Sciences, grant number SKLLQG2103.

Data Availability Statement: Not applicable.

Conflicts of Interest: The authors declare no conflict of interest.

References

1. Zheng, C.; Li, X.; Li, J.; Duan, J.; Wu, H.; Zhu, F. Investigation on the ammonia emission characteristics in coal-fired power plants of China. *Fuel* **2022**, *314*, 123046–123054. [CrossRef]
2. Chen, C.; Shen, A.; Duan, Y.; Meng, J.; Hu, B.; Tan, H.; Ruan, R.; Liu, X.; Liu, M. Removal characteristics of particulate matters and hazardous trace elements in a 660 MW ultra-low emission coal-fired power plant. *Fuel* **2022**, *311*, 122535–122545. [CrossRef]
3. Chen, J.H.; Tseng, T.H.; Ho, Y.C.; Lin, H.H.; Lin, W.L.; Wang, C.J. Gaseous nitrogen oxides stimulate cell cycle progression by retinoblastoma phosphorylation via activation of cyclins/Cdks. *Toxicol. Sci.* **2003**, *76*, 83–90. [CrossRef] [PubMed]

4. Jia, Y.; Jiang, J.; Zheng, R.; Guo, L.; Yuan, J.; Zhang, S.; Gu, M. Insight into the reaction mechanism over PMoA for low temperature NH_3-SCR: A combined In-situ DRIFTs and DFT transition state calculations. *J. Hazard. Mater.* **2021**, *412*, 125258–125272. [CrossRef]
5. Cao, J.; Rohani, S.; Liu, W.; Liu, H.; Lu, Z.; Wu, H.; Jiang, L.; Kong, M.; Liu, Q.; Yao, X. Influence of phosphorus on the NH_3-SCR performance of CeO_2-TiO_2 catalyst for NO_x removal from co-incineration flue gas of domestic waste and municipal sludge. *J. Colloid Interface Sci.* **2022**, *610*, 463–473. [CrossRef] [PubMed]
6. Chen, J.; Guo, L.; Zhu, H.; Qiu, Y.; Yin, D.; Zhang, T.; Chen, J.; Peng, Y.; Li, J. Balancing redox and acidic properties for optimizing catalytic performance of SCR catalysts: A case study of nanopolyhedron CeO_x-supported WO_x. *J. Environ. Chem. Eng.* **2021**, *9*, 105828–105838. [CrossRef]
7. Kubota, H.; Toyao, T.; Maeno, Z.; Inomata, Y.; Murayama, T.; Nakazawa, N.; Inagaki, S.; Kubota, Y.; Shimizu, K.-I. Analogous Mechanistic Features of NH_3-SCR over Vanadium Oxide and Copper Zeolite Catalysts. *ACS Catal.* **2021**, *11*, 11180–11192. [CrossRef]
8. Croisé, C.; Pointecouteau, R.; Akil, J.; Demourgues, A.; Bion, N.; Courtois, X.; Can, F. Insight into the praseodymium effect on the NH_3-SCR reaction pathways over W or Nb supported ceria-zirconia based catalysts. *Appl. Catal. B Environ.* **2021**, *298*, 120563–120576. [CrossRef]
9. Liu, K.; He, H.; Chu, B. Microkinetic study of NO oxidation, standard and fast NH_3-SCR on $CeWO_x$ at low temperatures. *Chem. Eng. J.* **2021**, *423*, 130128–130140. [CrossRef]
10. Li, M.; Sakong, S.; Groß, A. In Search of the Active Sites for the Selective Catalytic Reduction on Tungsten-Doped Vanadia Monolayer Catalysts Supported by TiO_2. *ACS Catal.* **2021**, *11*, 7411–7421. [CrossRef]
11. Wang, X.; Lei, Y.; Yan, L.; Liu, T.; Zhang, Q.; He, K. A unit-based emission inventory of SO_2, NO_x and PM for the Chinese iron and steel industry from 2010 to 2015. *Sci. Total Environ.* **2019**, *676*, 18–30. [CrossRef]
12. Zhao, S.; Shi, J.-W.; Niu, C.; Wang, B.; He, C.; Liu, W.; Xiao, L.; Ma, D.; Wang, H.; Cheng, Y. $FeVO_4$-supported Mn–Ce oxides for the low-temperature selective catalytic reduction of NO_x by NH_3. *Catal. Sci. Technol.* **2021**, *11*, 6770–6781. [CrossRef]
13. Huang, X.; Dong, F.; Zhang, G.; Guo, Y.; Tang, Z. A strategy for constructing highly efficient yolk-shell Ce@Mn@TiO_x catalyst with dual active sites for low-temperature selective catalytic reduction of NO with NH_3. *Chem. Eng. J.* **2021**, *419*, 129572–129584. [CrossRef]
14. Lu, P.; Ye, L.; Yan, X.; Fang, P.; Chen, X.; Chen, D.; Cen, C. Impact of toluene poisoning on MnCe/HZSM-5 SCR catalyst. *Chem. Eng. J.* **2021**, *414*, 128838–128847. [CrossRef]
15. Ye, L.; Lu, P.; Chen, D.; Chen, D.; Wu, H.; Dai, W.; Gan, Y.; Xiao, J.; Xie, Z.; Li, Z.; et al. Activity enhancement of acetate precursor prepared on MnO_x-CeO_2 catalyst for low-temperature NH_3-SCR: Effect of gaseous acetone addition. *Chin. Chem. Lett.* **2021**, *32*, 2509–2512. [CrossRef]
16. Kang, K.; Yao, X.; Huang, Y.; Cao, J.; Rong, J.; Zhao, W.; Luo, W.; Chen, Y. Insights into the co-doping effect of Fe^{3+} and Zr^{4+} on the anti-K performance of $CeTiO_x$ catalyst for NH_3-SCR reaction. *J. Hazard. Mater.* **2021**, *416*, 125821–125833. [CrossRef] [PubMed]
17. Shi, Y.; Yi, H.; Gao, F.; Zhao, S.; Xie, Z.; Tang, X. Evolution mechanism of transition metal in NH_3-SCR reaction over Mn-based bimetallic oxide catalysts: Structure-activity relationships. *J. Hazard. Mater.* **2021**, *413*, 125361–125373. [CrossRef] [PubMed]
18. Meng, D.; Zhan, W.; Guo, Y.; Guo, Y.; Wang, L.; Lu, G. A Highly Effective Catalyst of Sm-MnO_x for the NH_3-SCR of NO_x at Low Temperature: Promotional Role of Sm and Its Catalytic Performance. *ACS Catal.* **2015**, *5*, 5973–5983. [CrossRef]
19. Zhang, N.; Li, L.; Guo, Y.; He, J.; Wu, R.; Song, L.; Zhang, G.; Zhao, J.; Wang, D.; He, H. A MnO_2-based catalyst with H_2O resistance for NH_3-SCR: Study of catalytic activity and reactants-H_2O competitive adsorption. *Appl. Catal. B Environ.* **2020**, *270*, 118860–118875. [CrossRef]
20. Yuan, H.; Sun, N.; Chen, J.; Jin, J.; Wang, H.; Hu, P. Insight into the NH_3-Assisted Selective Catalytic Reduction of NO on β-MnO_2(110): Reaction Mechanism, Activity Descriptor, and Evolution from a Pristine State to a Steady State. *ACS Catal.* **2018**, *8*, 9269–9279. [CrossRef]
21. Zhang, B.; Liebau, M.; Suprun, W.; Liu, B.; Zhang, S.; Gläser, R. Suppression of N_2O formation by H_2O and SO_2 in the selective catalytic reduction of NO with NH_3 over a Mn/Ti–Si catalyst. *Catal. Sci. Technol.* **2019**, *9*, 4759–4770. [CrossRef]
22. Wang, D.; Yao, Q.; Mou, C.; Hui, S.; Niu, Y. New insight into N_2O formation from NH_3 oxidation over MnO/TiO_2 catalyst. *Fuel* **2019**, *254*, 115719–115725. [CrossRef]
23. Fan, H.; Fan, J.; Chang, T.; Wang, X.; Wang, X.; Huang, Y.; Zhang, Y.; Shen, Z. Low-temperature Fe–MnO_2 nanotube catalysts for the selective catalytic reduction of NO_x with NH_3. *Catal. Sci. Technol.* **2021**, *11*, 6553–6563. [CrossRef]
24. Jiang, Z.; Zou, Y.; Li, Y.; Kong, F.; Yang, D. Environmental life cycle assessment of supercapacitor electrode production using algae derived biochar aerogel. *Biochar* **2021**, *3*, 701–714. [CrossRef]
25. Liu, L.; Wang, B.; Yao, X.; Yang, L.; Jiang, W.; Jiang, X. Highly efficient MnO_x/biochar catalysts obtained by air oxidation for low-temperature NH_3-SCR of NO. *Fuel* **2021**, *283*, 119336–119343. [CrossRef]
26. Hou, Y.; Liang, Y.; Hu, H.; Tao, Y.; Zhou, J.; Cai, J. Facile preparation of multi-porous biochar from lotus biomass for methyl orange removal: Kinetics, isotherms, and regeneration studies. *Bioresour. Technol.* **2021**, *329*, 124877–124883. [CrossRef]
27. Xu, X.; Guo, Y.; Shi, R.; Chen, H.; Du, Y.; Liu, B.; Zeng, Z.; Yin, Z.; Li, L. Natural Honeycomb-like structure cork carbon with hierarchical Micro-Mesopores and N-containing functional groups for VOCs adsorption. *Appl. Surf. Sci.* **2021**, *565*, 150550–150559. [CrossRef]
28. Chen, L.; Yang, J.; Ren, S.; Chen, Z.; Zhou, Y.; Liu, W. Effects of Sm modification on biochar supported Mn oxide catalysts for low-temperature NH_3-SCR of NO. *J. Energy Inst.* **2021**, *98*, 234–243. [CrossRef]

29. Yang, J.; Su, Z.; Ren, S.; Long, H.; Kong, M.; Jiang, L. Low-temperature SCR of NO with NH_3 over biomass char supported highly dispersed Mn-Ce mixed oxides. *J. Energy Inst.* **2019**, *92*, 883–891. [CrossRef]
30. Fan, H.; Shen, Z.; Wang, X.; Fan, J.; Sun, J.; Chang, T.; Huang, Y.; Wang, X.; Sun, J. Kiwi twig biochar recycling promoting the reduction of NO by a MnO_2 catalyst. *Appl. Surf. Sci.* **2022**, *596*, 153644. [CrossRef]
31. Xiong, X.; Yu, I.K.M.; Dutta, S.; Masek, O.; Tsang, D.C.W. Valorization of humins from food waste biorefinery for synthesis of biochar-supported Lewis acid catalysts. *Sci. Total Environ.* **2021**, *775*, 145851–145858. [CrossRef] [PubMed]
32. Yuan, S.; Dong, B.; Dai, X. Facile and scalable synthesis of high-quality few-layer graphene from biomass by a universal solvent-free approach. *Appl. Surf. Sci.* **2021**, *562*, 150203–150210. [CrossRef]
33. Nanda, S.S.; Kim, M.J.; Yeom, K.S.; An, S.S.A.; Ju, H.; Yi, D.K. Raman spectrum of graphene with its versatile future perspectives. *TrAC Trends Anal. Chem.* **2016**, *80*, 125–131. [CrossRef]
34. Zhou, Q.; Zhao, Z.; Zhang, Y.; Meng, B.; Zhou, A.; Qiu, J. Graphene Sheets from Graphitized Anthracite Coal: Preparation, Decoration, and Application. *Energy Fuel* **2012**, *26*, 5186–5192. [CrossRef]
35. Zhang, Y.; Liu, Y.; Liu, Z.; Wu, X.; Wen, Y.; Chen, H.; Ni, X.; Liu, G.; Huang, J.; Peng, S. MnO_2 cathode materials with the improved stability via nitrogen doping for aqueous zinc-ion batteries. *J. Energy Chem.* **2022**, *64*, 23–32. [CrossRef]
36. Sun, X.; Shi, Y.; Zhang, W.; Li, C.; Zhao, Q.; Gao, J.; Li, X. A new type Ni-MOF catalyst with high stability for selective catalytic reduction of NO_x with NH_3. *Catal. Commun.* **2018**, *114*, 104–108. [CrossRef]
37. Saha, S.; Pal, A. Microporous assembly of MnO_2 nanosheets for malachite green degradation. *Sep. Purif. Technol.* **2014**, *134*, 26–36. [CrossRef]
38. Shi, X.; Guo, J.; Shen, T.; Fan, A.; Yuan, S.; Li, J. Enhancement of Ce doped La–Mn oxides for the selective catalytic reduction of NO_x with NH_3 and SO_2 and/or H_2O resistance. *Chem. Eng. J.* **2021**, *421*, 129995–130005. [CrossRef]
39. Jiang, H.; Wang, Q.; Wang, H.; Chen, Y.; Zhang, M. MOF-74 as an Efficient Catalyst for the Low-Temperature Selective Catalytic Reduction of NO_x with NH_3. *ACS Appl. Mater. Inter.* **2016**, *8*, 26817–26826. [CrossRef]
40. Du, H.; Han, Z.; Wu, X.; Wang, Q.; Li, C.; Gao, Y.; Yang, S.; Song, L.; Dong, J.; Pan, X. Enhancement effects of Er modification on comprehensive performance of FeMn/TiO_2 catalysts for selective reduction of NO with NH_3 at low temperature. *J. Environ. Chem. Eng.* **2021**, *9*, 105653–105666. [CrossRef]
41. Chen, L.; Yao, X.; Cao, J.; Yang, F.; Tang, C.; Dong, L. Effect of Ti^{4+} and Sn^{4+} co-incorporation on the catalytic performance of CeO_2-MnO_x catalyst for low temperature NH_3-SCR. *Appl. Surf. Sci.* **2019**, *476*, 283–292. [CrossRef]
42. Liu, Z.; Tian, X.; Xu, X.; He, L.; Yan, M.; Han, C.; Li, Y.; Yang, W.; Mai, L. Capacitance and voltage matching between MnO_2 nanoflake cathode and Fe_2O_3 nanoparticle anode for high-performance asymmetric micro-supercapacitors. *Nano Res.* **2017**, *10*, 2471–2481. [CrossRef]
43. Xu, H.; Qu, Z.; Zhao, S.; Mei, J.; Quan, F.; Yan, N. Different crystal-forms of one-dimensional MnO_2 nanomaterials for the catalytic oxidation and adsorption of elemental mercury. *J. Hazard. Mater.* **2015**, *299*, 86–93. [CrossRef] [PubMed]
44. Shi, Q.; Liu, T.; Li, Q.; Xin, Y.; Lu, X.; Tang, W.; Zhang, Z.; Gao, P.-X.; Anderson, J.A. Multiple strategies to decrease ignition temperature for soot combustion on ultrathin MnO_{2-x} nanosheet array. *Appl. Catal. B Environ.* **2019**, *246*, 312–321. [CrossRef]
45. Chen, B.; Wu, B.; Yu, L.; Crocker, M.; Shi, C. Investigation into the Catalytic Roles of Various Oxygen Species over Different Crystal Phases of MnO_2 for C_6H_6 and HCHO Oxidation. *ACS Catal.* **2020**, *10*, 6176–6187. [CrossRef]
46. Gong, P.; Xie, J.; Fang, D.; Han, D.; He, F.; Li, F.; Qi, K. Effects of surface physicochemical properties on NH_3-SCR activity of MnO_2 catalysts with different crystal structures. *Chin. J. Catal.* **2017**, *38*, 1925–1934. [CrossRef]
47. Fang, D.; Xie, J.; Hu, H.; Yang, H.; He, F.; Fu, Z. Identification of MnO_x species and Mn valence states in MnO_x/TiO_2 catalysts for low temperature SCR. *Chem. Eng. J.* **2015**, *271*, 23–30. [CrossRef]
48. Niu, C.; Wang, B.; Xing, Y.; Su, W.; He, C.; Xiao, L.; Xu, Y.; Zhao, S.; Cheng, Y.; Shi, J. Thulium modified MnO_x/TiO_2 catalyst for the low-temperature selective catalytic reduction of NO with ammonia. *J. Clean. Prod.* **2021**, *290*, 125858–125869. [CrossRef]
49. Yao, X.; Chen, L.; Cao, J.; Yang, F.; Tan, W.; Dong, L. Morphology and Crystal-Plane Effects of CeO_2 on TiO_2/CeO_2 Catalysts during NH_3-SCR Reaction. *Ind. Eng. Chem. Res.* **2019**, *57*, 12407–12419. [CrossRef]
50. Wang, J.; Yan, Z.; Liu, L.; Chen, Y.; Zhang, Z.; Wang, X. In situ DRIFTS investigation on the SCR of NO with NH_3 over V_2O_5 catalyst supported by activated semi-coke. *Appl. Surf. Sci.* **2014**, *313*, 660–669. [CrossRef]